Lithuanian Journal of Physics, Vol. **62**, No. 4, pp. 254–266 (2022)
© Lietuvos mokslų akademija, 2022

OPTIMIZATION OF TERAHERTZ DETECTORS BASED ON GRAPHENE FIELD EFFECT TRANSISTORS BY HIGH IMPEDANCE ANTENNAE

D. Vizbaras [a], K. Ikamas [a, c], S. Pralgauskaitė [a], J. Matukas [a],

A.A. Generalov [d], and A. Lisauskas [a, b]

[a] *Institute of Applied Electrodynamics and Telecommunications, Vilnius University, Saulėtekio 3, 10257 Vilnius, Lithuania*

[b] *CENTERA Laboratories, Institute of High Pressure Physics PAS, Warsaw, 01-142 Poland*

[c] *Research Group on Logistics and Defense Technology Management, General Jonas Žemaitis Military Academy of Lithuania, Šilo 5, 10322 Vilnius, Lithuania*

[d] *VTT Technical Research Centre of Finland LTD, P.O. Box 1000, FI-02044 VTT*

Email: domantas.vizbaras@ff.vu.lt

Received 23 October 2022; accepted 23 October 2022

This contribution presents the results of investigations performed on monolayer graphene field effect transistor-based (GFET-based) terahertz detectors. We have implemented three different types of planar antennae: a bow-tie, a bow-tie with transmission lines and a slot-disc, allowing us to realize different conditions for high-frequency impedance matching. We present a semi-empirical model which uses physical parameters derived from electrical characterization results of devices and electrodynamic characteristics of antennae, allowing us to predict THz responsivity. Model predictions have been compared with the responsivity measurements performed at room temperature in a frequency range from 50 to 1250 GHz. Good agreement between the model predictions and experimental results implies the eligibility of a distributed resistive mixing approximation for GFET. In addition, the device stability, the temperature dependence and the origin of noise in the transistor channel have been investigated. Finally, to the best of our knowledge, we demonstrate the record performance values for room temperature graphene-based terahertz detectors: 80V/W optical responsivity without the normalization to the antenna effective area and a noise equivalent power of 111 pW/$\sqrt{\text{Hz}}$ at 336 GHz.

Keywords: power detectors, field effect transistor (FET), graphene, submillimeter wave measurements, terahertz (THz), hysteresis, analytical model

1. Introduction

Graphene is a two-dimensional allotrope of carbon consisting of a single layer of atoms. Due to its distinguishing characteristics, such as linear energy dispersion and a zero band gap, charge carriers can achieve room temperature mobility of up to $4 \cdot 10^4$ cm^2/V·s [1] together with an extraordinary saturation velocity, which can get much higher values than that of silicon [2]. Thus, graphene field effect transistors (GFETs) are considered to become serious contenders in the field of terahertz (0.1–10 THz range) electronics. Furthermore, the exceptional ratio between the surface area and volume makes graphene-based devices a promising technology for gas sensing [3, 4], or as biosensors in non-ionizing medical imaging or security screening [5–8].

The technology of GFET-based detectors has come a long way during the last decade. The best results of a single transistor measured at room temperature (RT) so far were published in 2017, reporting the maximum optical responsivity of 74 V/W and the noise equivalent power (NEP) of 130 pW/$\sqrt{\text{Hz}}$

at 400 GHz [9]. Despite already achieved good performance values, GFETs are still heavily outshined by silicon-based detectors [10]. This is due to some serious, still unsolved, issues with GFET detectors. One is a high contact resistance arising from graphene–metal contact [11]. It has been an object for investigation for a while, and there are several strategies for improvements [12, 13]. However, other aspects of GFET THz detectors have been discussed less because of their not-so-apparent impact. This includes the drift of GFET characteristics over time when exposed to air [14], or the influence of temperature on a device performance [15].

In this paper, we explore multiple aspects of the operation of state-of-the-art GFET THz detectors. In order to address the peculiarities of GFET THz detector operation, we carried out experiments on devices connected to three different antenna types. Further, we discuss applied measurement techniques and the model employed for the simulation of THz responsivity. Then we present static detector GFET characteristics, noise and stability issues, and GFET THz detector characteristics such as voltage responsivity and noise equivalent power (NEP).

2. Design of detectors

The mono-layer graphene sheets used in this study were grown by chemical vapour deposition on a copper foil and processed at *VTT* (Finland). Graphene was transferred onto a high-resistivity silicon wafer with a 300 nm SiO_2 layer. Al_2O_3, grown by atomic layer deposition, is used as a gate dielectric. The series of devices with a channel length from 0.5 to 2.5 μm have been produced. The source and drain contacts were evaporated using Ti/Au directly on graphene, whereas another evaporated layer of Ti/Au on Al_2O_3 is used as a gate metal. The height of all metallic layers is 100 nm.

The metalization of contact areas plays a major role in the interaction of micrometer and sub-micrometer scale devices with THz radiation. Therefore, effective interaction can be achieved if contact metalization is embedded into the antenna structure. For this study we implemented three different types of antennas. These antennas are displayed in Fig. 1. One is a resonant slot-dipole antenna (Fig. 1(c)) designed for optimum response at 240 GHz frequency. The other two are broadband bow-tie antennas. Antenna (b) was designed with metal transmission lines to increase the impedance of the bow-tie so that it could better match the impedance of the transistor channel. In theory, this is supposed to lower the power transfer losses of the GFET–antenna interface and increase the detector responsivity (see Section 4). The antenna characteristics were electromagnetically simulated using the *Keysight* ADS and *Ansys* HFSS software. The physical parameters of investigated samples and their characteristical electrical parameters are summarized in Table 1.

3. Measurement setups

The quasi-static (dc) detector performance was evaluated at room temperature, atmospheric pressure and in an electromagnetically shielded room to reduce the effect of external noise sources. The channel resistance and electrical transfer characteristics were measured with a *Keysight* B1500A semiconductor analyzer. Furthermore, the electrical characteristics have been measured over a wide temperature range from 77 to 295 K in a temperature-controlled, nitrogen-cooled cryostat.

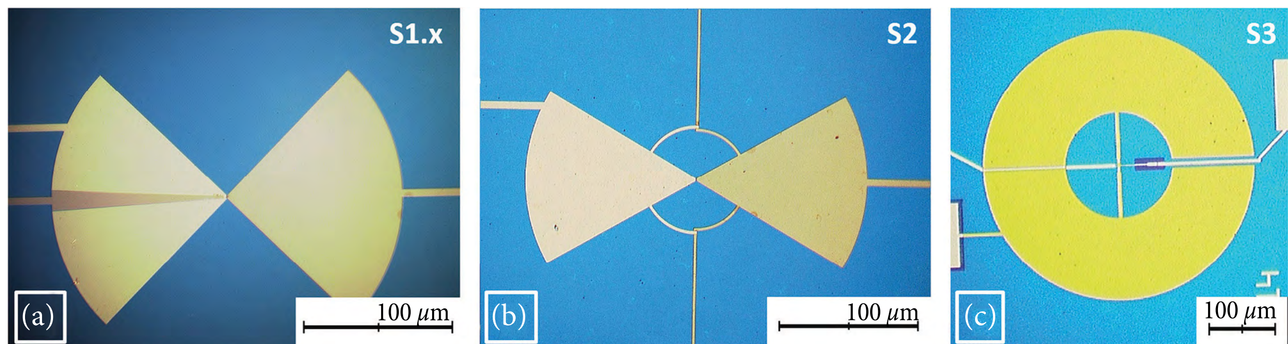

Fig. 1. GFET detector antennas: (a) broadband bow-tie antenna (marked as S1.x); (b) broadband bow-tie antenna with transmission lines (S2); (c) resonant slot-dipole (S3).

Table 1. Parameters and physical characteristics of samples derived by fitting the measured static channel resistance.

Sample code	Antenna type	Channel length, μm	Gate width, μm	Gate oxide height, nm	Contact resistance, Ω	Threshold voltage V_{th}, V	Mobility of electrons, cm²/V·s
S1.1	Bow-tie	2.5	2	20	1314	–0.16	3315
S1.2	Bow-tie	2.5	2	20	2863	–0.46	2237
S1.3	Bow-tie	2.5	2	20	1157	–1.31	1450
S2	Bow-tie with transmission lines	2	2	20	2247	–0.52	2506
S3	Slot-disc	0.5	4	30	1048	–1.24	1918

The device packaging procedure included several steps. In the first, the dies with six THz detectors were glued to 0.5 mm thick high-resistivity silicon wafers. Then the silicon carrier was glued to a PCB, and the devices were ultrasonically bonded to bonding pads using a 25 μm diameter Al wire. This packaging strategy was selected to form a sliding contact between the die with electrically connected devices and the hyper hemispheric silicon lens. It allowed us to align each detector on the die into the focus of the incoming THz beam. Two different sources of THz radiation were employed: an electronic frequency multiplier from *Virginia Diodes Inc.* and a broadband photomixer-based source from the *Toptica GmbH* Terascan 1500 system. The detector module and THz source were assembled into a 4-F optical system shown in Fig. 2. The Gaussian THz beam was first collimated with a 4 inch off-axis parabolic mirror (OAP) and then attenuated by two thin films coated with chrome when an electronic multiplier was used to avoid detector saturation and suppress standing waves. Finally, another OAP focused the beam onto the substrate lens, which was then used to tighter focus the beam on the detector antenna. This setup allowed us to characterize devices in several frequency sets, partially covering the 170–750 GHz range (and seamless covering from 50 to 1250 GHz using a *Toptica GmbH* photomixer). We used a large aperture detector from *Thomas Keating Ltd.* to calibrate available THz power. A low-noise voltage preamplifier was used to condition the signal and protect samples against electrostatic discharges.

To obtain detector voltage responsivity ($\Re_V$), the obtained detector voltage response (V_{det}) was divided by the incident power (P_{in}) measured with the reference detector:

$$\Re_V = \frac{V_{det}}{P_{in}}. \quad (1)$$

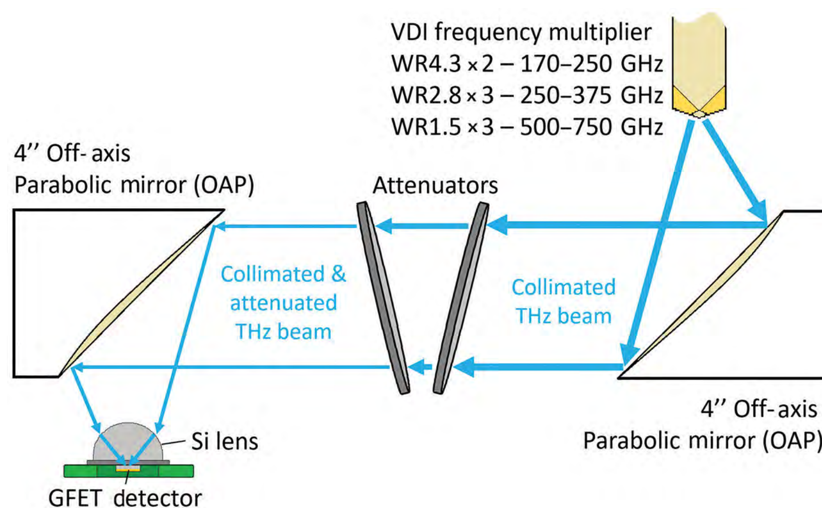

Fig. 2. The setup used for calibrated measuring device response to THz radiation characteristics.

The second important detector optical performance parameter is the noise-equivalent power or NEP. It is calculated by dividing noise spectral density by responsivity:

$$NEP = \frac{\sqrt{4k_B T R_{dc}}}{\Re_V}. \quad (2)$$

Here R_{dc} is the static GFET channel resistance, T is the ambient temperature, and k_B is the Boltzmann constant. For NEP calculations, the Johnson–Nyquist noise spectral density approximation was applied. The validity of this approximation is discussed in Section 6.

4. GFET simulation

The high-frequency modelling of the detector was performed using an in-house developed physics-based analytic model. It is grounded on a kernel describing the rectification process in the FET with the help of a distributed transmission line channel model [16, 17]. The voltage responsivity R_V of GFET-based detectors can be predicted from the electron branch of transistor channel resistance R_{ch} dependence on the gate voltage V_g and modelled high-frequency parameters,

$$\Re_V = -\frac{1}{4}\frac{\partial \ln R_{ch}}{\partial V_g} \times \left[1 + \frac{2\omega\tau}{\sqrt{1+(\omega\tau)^2}}\right] 8\,\mathrm{Re}(Z_A) H^2 \eta, \quad (3)$$

with $R_{ch} = R_{dc} - R_s - R_d$, where R_g, R_s, R_d are gate, source and drain contact resistances, respectively. Z_A is the antenna impedance, ω is the angular frequency of the THz wave, and τ is the electron momentum scattering time. η combines the antenna efficiency factor and other possible THz radiation coupling loss mechanisms. $f(\omega,\tau) = 1 + 2\omega\tau / \sqrt{1+(\omega\tau)^2}$ is the efficiency factor firstly introduced in Ref. [18]. For a nonresonant case, when $s\tau/L_g \ll 1$ (L_g is the gate length, s is the electron plasma velocity), f describes the device ablity to convert THz power to signal relative to that of low-frequency resistive mixing [19]. The voltage attenuation factor H accounts for the mismatching between the antenna impedance Z_A and the transistor channel impedance Z_{ch}:

$$H = \left|\frac{Z_{ch}}{Z_{ch} + Z_A + R_g + R_s}\right|. \quad (4)$$

Equations (3) and (4) are derived for the detector which involves a single transistor architecture. Almost all detectors presented here are based on this architecture except one sample with a slot-disc antenna (S3). In this device, antenna leaves are connected with two transistors to achieve the asymmetric power coupling into channels, which is an essential condition for an efficient plasma-wave rectification [20]. For this case, Eq. (4) must be modified, changing the term Z_A to $Z_A/4$, which reflects the fact that the high-frequency current flows in series through transistor channels whereas the rectified signal currents are added.

The analytical model is partly based on quasistatic device parameters and fundamental physical quantities: the channel resistance R_{ch}, the impedances R_g and R_s representing the parts of the channel not controlled by the gate electrode, and the relaxation time τ. These characteristics can be derived from the measured transistor channel resistance R_{dc} dependence on the gate voltage V_g using the fit model based on a description of the gate-voltage dependent carrier density in the gated channel region of the FET derived from the unified charge-density control model [21, 22].

The fitting procedure gives the mobility of electrons μ instead of the relaxation time τ which is needed for the analytical model. For field effect transistors based on classical semiconductors, these two physical parameters are linked by a simple equation

$$\tau = m^*\mu/e, \quad (5)$$

where m^* is the effective mass of electrons and e is an elementary charge. Although the linear energy dispersion implies that quasiparticles are massless, an ensemble of electrons still moves with inertia having an equivalent role as effective mass $m^* = \hbar k_F/v_F$, where k_F, v_F are the Fermi wave vector and Fermi velocity, respectively [23, 24]. In this case, m^* depends on the density of charge carriers, i.e. gate voltage in FET, and our analytical model (3) must be revised. For the estimation of detector performance we used a simpler approach – an experimentally derived effective mass of monolayer graphene $m^* = 0.012\, m_e$, where m_e is a free-electron mass [25].

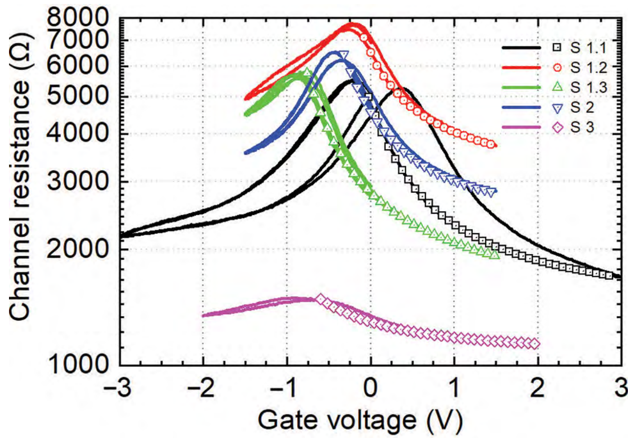

Fig. 3. The drain-source resistance of the GFET versus the gate voltage. The symbols show the fit of the measured electron branch of resistance with a drift-diffusion model. S1.1–S1.3 are the samples with the bow-tie antenna, S2 is the bow-tie with transmission lines, and S3 is the slot-disc.

Figure 3 shows the results of the dc resistance measurements at a low source-drain voltage of 1 mV (solid lines) and the fitted curves (symbols). Only electron branches of the resistance curve (the right downward sweep direction) are fitted; however, the other sweep directions are included in the figure for completeness. The main parameters extracted from the fitting procedure are presented in Table 1 and are in good agreement with previous results obtained for similar samples [9].

The analytical model used the extracted parameters for further device simulation. The main results are presented in Fig. 4. The 1 mV amplitude of THz radiation, typical of the THz sources in the 250–1000 GHz band, was used for the calculations. The intrinsic responsivity (a) is calculated using Eq. (3) by replacing the incident power with the power directly absorbed in Z_{ch}. In this case, the term $8\text{Re}(Z_A)H^2\eta/R_{ch}$ is substituted by $(2\text{Re}(1/Z_{ch})R_{ch})^{-1}$. The model does not predict any plasmonic-related enhancements in device performance because the transistor channel is comparatively long despite short scattering time (plasma waves damping condition $s\tau/L_g \ll 1$ is satisfied for all measured samples). In reality, any transistor has several parasitic elements, such as contact resistance. These parasitics dissipate a part of the power entering the detector. When it is taken into account together with the impedance mismatching between the FET channel and antenna, the device performance characteristics are reduced significantly (compare (a) and (b) panels in Fig. 4). The antenna coupling factor η is assumed to be 0.074 (having simulated antenna efficiency ≈0.3, a Gaussian beam coupling efficiency of 0.7, a transmission at the Si surface of 0.7 and a scattering factor 0.5). The frequency-dependent antenna impedances Z_A were electromagnetically (EM) simulated using the commercially available method of moments solver [26].

The model predicts the best optical responsivity (Fig. 4(b)) for samples S2 and S3 due to the much higher impedance of the antenna (the bow-tie with transmission lines and the slot-disc, respectively).

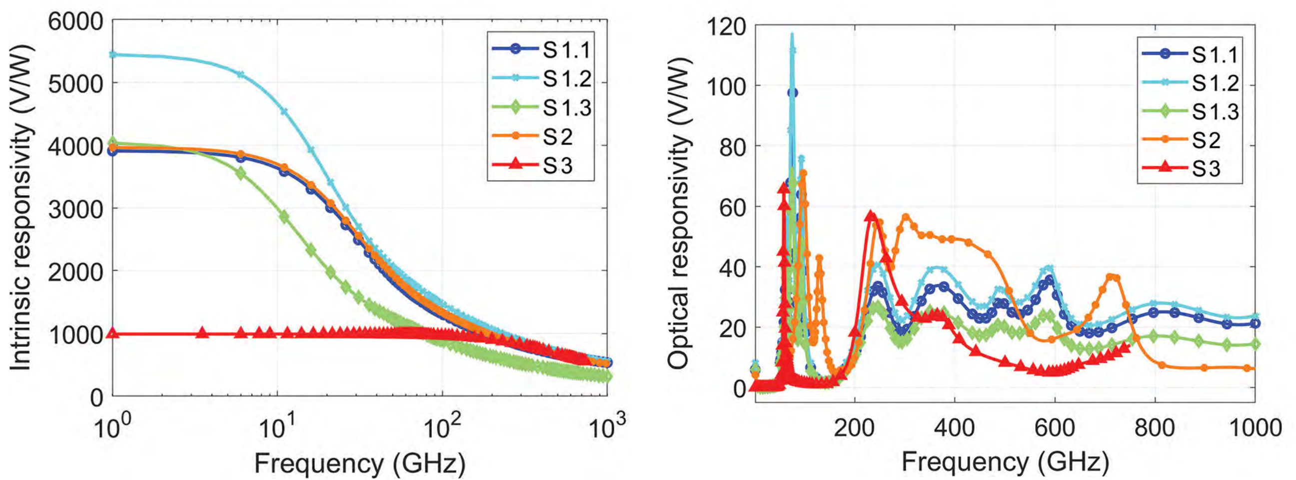

Fig. 4. Modelled voltage responsivity versus radiation frequency for the GFET samples used in the experiment. (a) Intrinsic responsivity does not account for the intrinsically absorbed power and the antenna coupling. These effects substantially change the optical responsivity dependence on the frequency (b). S1.1–S1.3 are the samples with the bow-tie antenna, S2 is the bow-tie with the transmission lines antenna, and S3 is the slot-disc antenna.

Samples S1.1, S1.2 and S1.3 have the simple bow-tie antenna, but their performance is determined by the contact resistance and the change in channel conductivity versus the gate voltage $\partial R_{ch}/V_g$. The last one can be visually estimated as a channel resistance difference between the Dirac point and a fully opened state (the maximum and minimum point on the right branch of the curve, Fig. 3). From this perspective, sample S1.2 looks the most promising in its category.

5. Influence of temperature and vacuum on channel resistance

A known issue with GFETs is their hysteretic behaviour depending on the voltage sweep direction, e.g. due to charging of defect states in the used materials [27, 28]. The device stability can be improved by putting samples in a vacuum environment and treating them with low temperatures. The measured source-drain resistance temperature dependences for one sample (S1.2) are displayed in Fig. 5. The coloured part of the graph shows how the GFET channel resistance changed while warming the detector from 77 K to room temperature. For comparison, the gray and black curves show the resistance measured before cooling, at RT, in air and in a vacuum, respectively. An immediate improvement in the GFET characteristics can be seen. After cooling the detector to liquid nitrogen temperatures and returning it to RT, the Dirac point of the GFET shifts closer to the zero gate voltage. This and the reduction in resistance hysteresis show that when cooled,

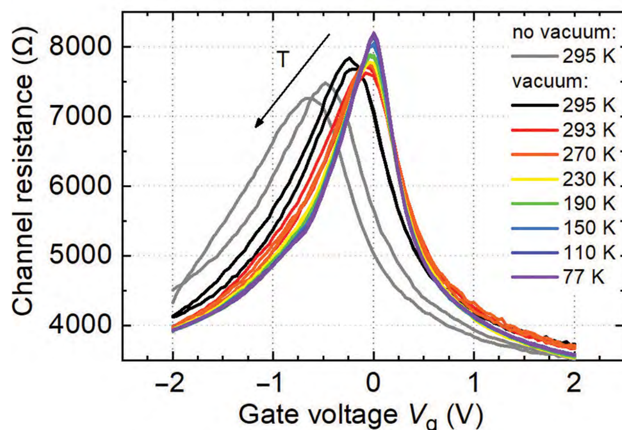

Fig. 5. Measured GFET channel resistance dependence on temperature. The sample is S1.2 (with bow-tie antenna).

the GFET loses its doping by substrate and air adsorbates [28]. When warming to RT in a vacuum, the detector can only get doped by the substrate and no longer by the adsorbates in the air. This result is like those achieved by annealing GFET THz detectors while heating them in a vacuum [15].

6. GFET channel noise

One factor that impacts the responsivity of GFET-based detectors is low-frequency noise. Most investigations found that a $1/f^{\alpha}$ noise dominates in GFETs at any bias, and Lorentzian type spectra are not observed usually [29, 30, 7, 31–33]. It is shown that the $1/f^{\alpha}$ noise intensity is proportional to the number of defects and impurities [31]. Therefore, the $1/f^{\alpha}$ type noise is caused by the superposition of many charge carrier trapping-detrapping processes. However, a certain defect-formed trapping centre can be more active than other processes and cause the Lorentzian noise spectrum [8]. This is inconvenient when making high responsivity detectors. Since thermal noise is the lowest possible noise level, reducing other noise sources should be the priority.

Low frequency (10 Hz – 100 kHz) fluctuations of GFETs were investigated at room temperature. The measured samples have $1/f^{\alpha}$ electrical fluctuations when current flows through the channel (Fig. 6(a)). As seen in the figure, the $1/f^{\alpha}$ noise does not depend on the flowing current or its direction. Nevertheless, when no current flows through the channel, only thermal fluctuations are observed at the zero bias (Fig. 6(b)). This feature is important as GFETs can be employed as detectors without bias [34], and the absence of noise sources other than thermal shows their potential as sensitive THz detectors.

In the general case, $1/f^{\alpha}$ noise spectra are observed when there are a lot of charge carrier trapping centres of similar activity with widely distributed characteristic times. The in-depth study of the peculiarities of $1/f^{\alpha}$ type noise can be used to determine the source of resistance fluctuation, which, in the case of graphene at cryogenic temperatures and magnetic fields, recently reopened a discussion of fluctuating mobility as a resistance determining parameter [35]. The noise spectra, measured in our devices at room temperature conditions, indicate the presence of traps with

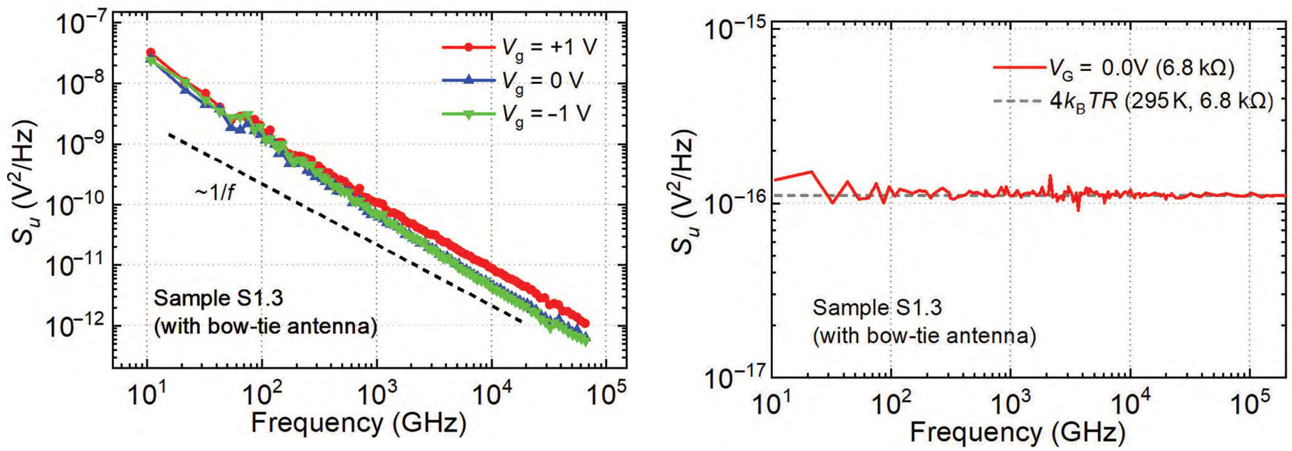

Fig. 6. The voltage noise spectral density dependence on the frequency for the graphene-based transistor when the drain current is 0.19 mA (a) and zero (b). The sample is S1.2 (with bow-tie antenna).

times from tens of microseconds to hundreds of milliseconds (Fig. 6(a)). However, the directly measured resistance variations in time show that much slower charge carrier trapping-detrapping processes are also present (Fig. 7). A different dynamic of resistance is observed at different bias voltages (their values and polarities) when measurements are performed in the air and vacuum. Such instabilities of characteristics indicate defects in the investigated structures with different time constants that can be quite large: from a few seconds to minutes and hours. Similar instabilities

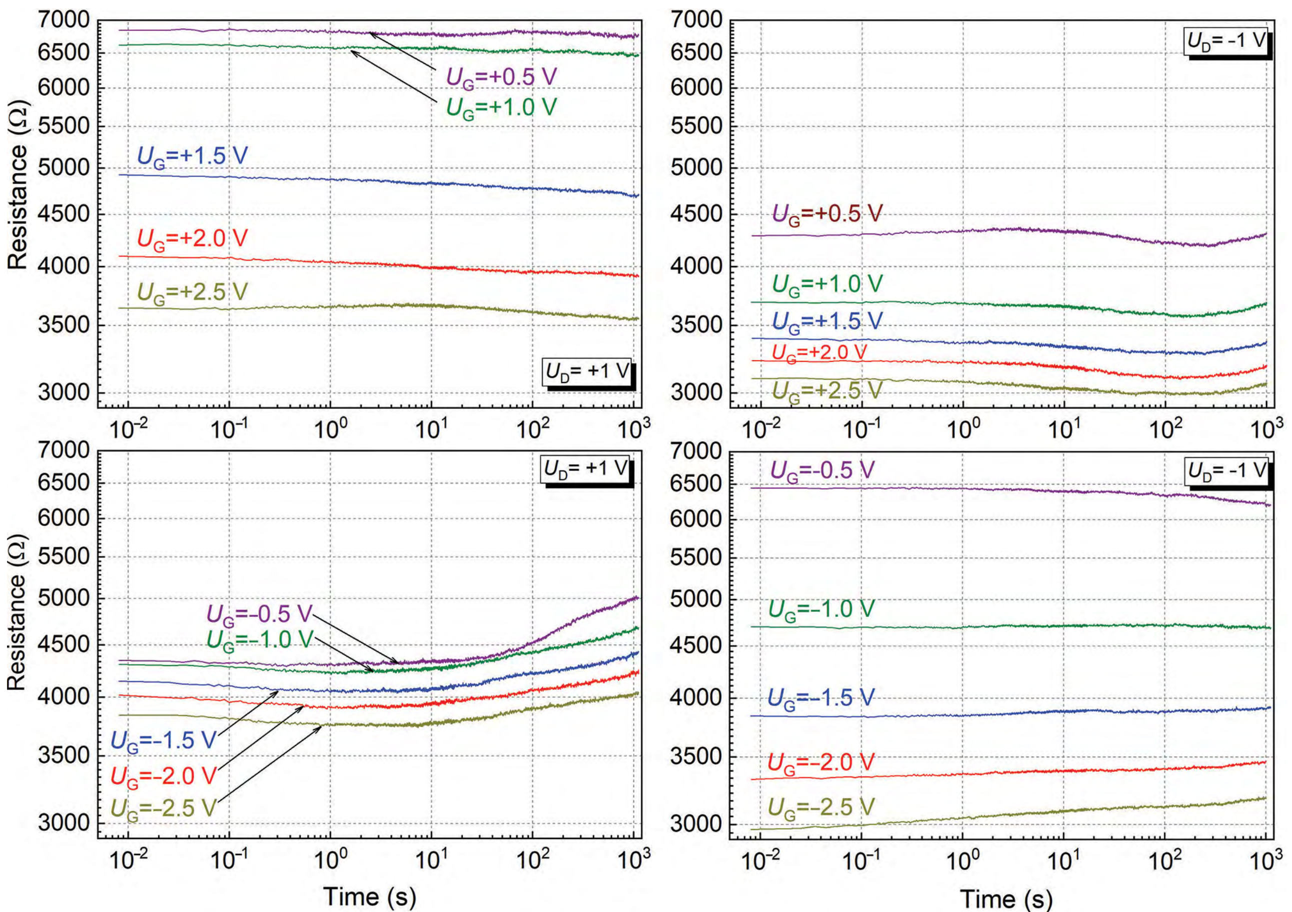

Fig. 7. The resistance variation in time at different biases at room temperature. The sample is S1.2 (with bow-tie antenna).

with long characteristic times were observed in AlGaN/GaN heterostructures [36, 37]. The resistance variations calculated from the measurements performed in the air atmosphere differ from when the device was in a vacuum. It suggests that impurities from the air are an important source of these instabilities.

7. Optical performance of detectors

This section discusses GFET THz detector NEP parameters and their dependences on frequency, transistor gate voltage and antenna types. For a better comparison, the NEP of simulated devices is presented.

The NEP–frequency dependence of a detector S1.2 with a bow-tie antenna is displayed in Fig. 8(a). We measured the detector response using two setups with different source types: an electronic multiplier (blue line) and a broadband photomixer (red line). Equations (1) and (2) and static channel resistance measurement results were used to calculate device performance characteristics. Two major valleys near 220 and 350 GHz and the position of one minor minimum near 800 GHz go well with the modelled ones (a grey dashed line). Low-frequency parasitic valleys below 100 GHz are shifted by 20 GHz towards lower frequencies than expected ones. Discrepancies can be caused by an inaccurate device optical alignment and the setup peculiarities, which are discussed further. Since the used antenna has much lower impedances than the GFET at major frequencies except resonant peaks, it is expected that even though the detector is broadband, it will work better where the modelled impedance is highest. Another interesting characteristic is observed where GFET THz detector gate voltage changes affect its responsivity and, consequently, the noise equivalent power. The measurement at V_g = 0.8 V (a blue curve) reveals better NEP values and a slightly better agreement with the modelling results. Since the terms H and $\partial R_{ch}/V_g$ are the functions of the gate voltage, the changes of GFET biasing conditions turn into changes of the channel impedance, which can affect the frequency-dependent behaviour of the device.

Figure 8(b) shows the NEP dependence on the frequency for the detector with a bow-tie with transmission lines antenna. Three major valleys are observed near 112, 240 and 350 GHz (a red line). The semiempirical model predicts a similar qualitative behaviour but differs in positions of minima, numbers and absolute values. It can be explained by a higher antenna geometrical complexity. When the substrate Si lens and the antenna are aligned at different frequencies, the broadband characteristics of the device also change (compare red and black lines in Fig. 8(b)). This phenomenon must be examined more rigorously in the future.

Both detector types display deep valleys in the low-frequency range (near 70 GHz for S1.2 sample and 110 GHz for S2). They result from an interaction of THz radiation with metallic wires connected to antenna and contact pads (see

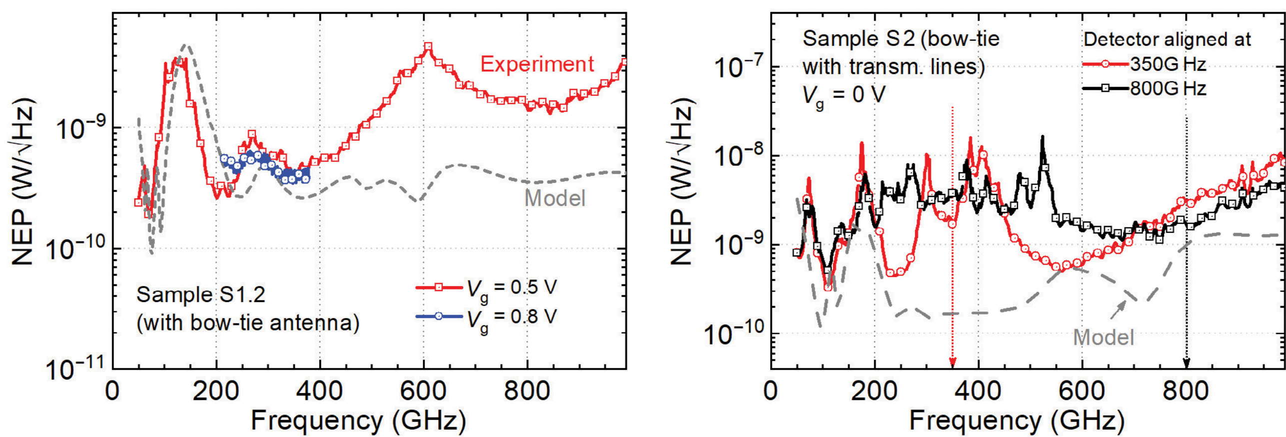

Fig. 8. The noise equivalent power vs the frequency of a GFET THz detector with the (a) bow-tie antenna and (b) bow-tie with transmission lines. The modelled values are depicted by a grey dashed line. In (a), the NEP calculation is based on measurements with two different sources: an electronic multiplier (a blue line) and a broadband photomixer (a red line).

the micrograph in Fig. 1(a)). The resonant frequency of parasitic dipoles can be estimated by taking the half-length of wires and the dielectric constant of a Si substrate ($\varepsilon_{eff} \approx 11.9$). For example, sample S1.2 has a dipole with a length of 700 μm, corresponding to the 72 GHz frequency.

For determination of the maximum detector responsivity and the minimum NEP, detector responses were measured while sweeping detector gate voltage. Figure 9 presents the NEP vs detector gate voltage characteristic of the best-tested GFET THz detector. Since NEP calculation involves detector channel resistance, it also has a hysteresis loop (compare with a black line in Fig. 3). Since the smallest NEP is very close to the zero-gate voltage, just as suggested in Section 6, GFET THz detectors could be used without bias and have the potential for high-sensitivity applications.

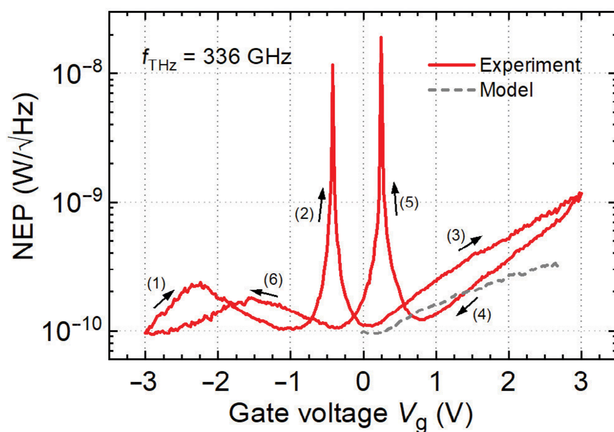

Fig. 9. The noise equivalent power dependency on the detector gate voltage. The sample is S1.1 (with bow-tie antenna). The numbers in brackets indicate the direction of the voltage sweep. The radiation frequency 336 GHz is the main resonant responsivity maximum of this sample. The grey dashed line shows the results of simulation based on the electron branch of resistance.

8. Discussion

The summary of the results from our studied devices is displayed in Table 2. The table also includes the state-of-the-art results on the GFET detectors performed with a similar methodology, i.e. using the total power of the beam. Regarding the overall results of our work, the so far achieved responsivity of 80 V/W and NEP of 111 pW/√Hz at room-temperature and 336 GHz are comparable and even slightly better than for the best reported GFET THz detectors. Our best device and both Refs. [9, 27] share the same antenna geometry and, therefore, the better performance could be only attributed to better impedance matching at a lower (336 GHz instead of 400 or 600 GHz) frequency. However, other our devices demonstrate responsivity and NEP values that are just about 10–50% of the best-reported results. This discrepancy could originate from the peculiarities of GFET fabrication which are responsible for the high spread of transistor electrical parameters.

The applied model shows that the transistor impedance starts a strong decrease for most samples before reaching the THz frequency limit (which loosely starts from 100 GHz, Fig. 4(a)). It is a consequence of the long channel of a few micrometres. It leads to a decrease in the responsivity of the detectors. Future applications would require GFETs with much shorter channels. A good example is sample S3 with a slot-disc antenna and a 0.5 μm long gate. Its simulated channel impedance remains high up to 200 GHz (see a red curve in Fig. 4(a)).

All tested GFETs demonstrated the hysteresis behaviour in the channel resistance measurements (Fig. 3). The analytical model uses two physical parameters of the transistor, the mobility and the resistance, which were obtained by fitting only the first electron branch of the *I–V* characteristics. This branch is obtained by sweeping the gate voltages toward the positive values. If we apply the same fitting procedure to the branch of reverse biasing direction, it results in different transistor parameters due to residual effects. For sample S1.1, the resistance drops from 1314 to 988 Ω, and the mobility drops by a factor of two (from 3315 to 1688 $cm^2/V\cdot s$). The analytical model with these parameters gives approximately 50% lower responsivity values, which better agree with the experimental results. Considering the hysteresis of *I–V* characteristics when modelling the GFET impedance response is necessary. As a first approximation, one can try to take the average of the physical parameters, but a solution that better deals with the physics of device operation is still required.

Internal plasmonic mixing is not the only mechanism responsible for the detector response

to THz radiation. There is much experimental evidence that a thermoelectric process can contribute to the device signal [38]. This effect can be one possible explanation for better NEP values in the hole branch of GFET (compare the right and the left side of Fig. 9). The signal below the zero gate voltage falls more slowly or not at all compared to the electron branches of the curve. A more comprehensive hydrodynamic transport description must be included in the analytical equations to model thermoelectric signal contribution to detection signals. It is out of the scope of this paper.

EM simulation and modelling of GFET detectors with a bow-tie with transmission lines and slot-disc antennae have shown high-performance characteristics. However, in the experiments, devices based on the new design proved worse than the reference design with the bow-tie. One possible explanation can be linked to the different hysteresis behaviour of detectors. The best sample demonstrated the strongest hysteresis both in *I*–*V* and THz response measurements (see Figs. 3 and 9). More rigorous experimental and theoretical investigations of the role of gate dielectric quality must be performed in the future. It is worth noting that new antenna designs with higher impedance did not result in devices with the best performance. However, because of considerably lower contact resistances achieved in these designs, we report decent performance despite the worse GFET characteristics of our tested devices. Therefore, these new designs still seem to be a promising step toward GFET THz detector performance optimization.

9. Conclusions

This work presents a comprehensive investigation of the electronic and optic characteristics of new terahertz detectors based on mono-layer graphene field effect transistors on a silicon oxide layer. In particular, we have implemented three different types of antenna: a bow-tie, a bow-tie with transmission lines and a slot-disc, allowing us to apply different high-frequency impedance matching conditions. A semi-empirical model that predicts the THz responsivity based on physical parameters derived from electrical characterizations and electrodynamic characteristics of the antenna was employed. The predictions of modelling results have been carefully compared with the experimental measurements, which include the determination of optical responsivity and noise equivalent power. The good agreement between modelling and experimental results implies the eligibility of a distributed resistive (in the limit of overdamped plasmonic excitation) mixing approximation for GFET. In addition, the device stability, the temperature dependence and the origin of noise in the transistor channel are investigated. Finally, to the best of our knowledge, the record values for room temperature graphene-based THz detectors graphene-based terahertz detectors: 80V/W optical responsivity without the normalization to the antenna effective area and a noise equivalent power of 111 pW/√Hz at 336 GHz were achieved.

Aknowledgements

The work was supported by the program 'Applicability and Commercialization of R&D Results' of

Table 2. Comparison of the responsivity and NEP of state-of-the-art GFET THz detectors measured without normalization at RT.

Frequency range, GHz	Antenna type	Maximum responsivity, V/W	Frequency of maximum responsivity, GHz	Minimum NEP, pW/√Hz	Ref.
50–1200	Bow-tie	80	336	111	This work
50–1200	Bow-tie with transmission lines	16	246	764	This work
150–380	Slot-dipole	9	250	1000	This work
130–450	Logarithmic spiral	20	130	600	[39]
400	Bow-tie	74	400	130	[9]
600	Bow-tie	14	600	515	[27]

Vilnius University Innovation Office. The Academy of Finland partly funded the work (Grant Nos. 343842 and 314809).

References

[1] J.-H. Chen, C. Jang, S. Xiao, M. Ishigami, and M.S. Fuhrer, Intrinsic and extrinsic performance limits of graphene devices on SiO_2, Nat. Nanotechnol. **3**(4), 206–209 (2008), https://doi.org/10.1038/nnano.2008.58

[2] M.A. Yamoah, W. Yang, E. Pop, and D. Goldhaber-Gordon, High-velocity saturation in graphene encapsulated by hexagonal boron nitride, ACS Nano **11**(10), 9914–9919 (2017), https://doi.org/10.1021/acsnano.7b03878

[3] S. Rumyantsev, G. Liu, M.S. Shur, R.A. Potyrailo, and A.A. Balandin, Selective gas sensing with a single pristine graphene transistor, Nano Lett. **12**(5), 2294–2298 (2012), https://doi.org/10.1021/nl3001293

[4] B. Kumar, K. Min, M. Bashirzadeh, A.B. Farimani, M.-H. Bae, D. Estrada, Y.D. Kim, P. Yasaei, Y.D. Park, E. Pop, N.R. Aluru, and A. Salehi-Khojin, The role of external defects in chemical sensing of graphene field-effect transistors, Nano Lett. **13**(5), 1962–1968 (2013), https://doi.org/10.1021/nl304734g

[5] G. Valušis, A. Lisauskas, H. Yuan, W. Knap, and H.G. Roskos, Roadmap of terahertz imaging 2021, Sensors **21**(12), 4092 (2021), https://doi.org/10.3390/s21124092

[6] Z. Cheng, Q. Li, Z. Li, Q. Zhou, and Y. Fang, Suspended graphene sensors with improved signal and reduced noise, Nano Lett. **10**(5), 1864–1868 (2010), https://doi.org/10.1021/nl100633g

[7] N.A.M. Tran, I. Fakih, O. Durnan, A. Hu, A.M. Aygar, I. Napal, A. Centeno, A. Zurutuza, B. Reulet, and T. Szkopek, Graphene field effect transistor scaling for ultra-low-noise sensors, Nanotechnology **32**(4), 045502 (2020), https://doi.org/10.1088/1361-6528/abc0c8

[8] J. Basu, A. Baral, N. Samanta, N. Mukherjee, and C. Roychaudhuri, Low noise field effect biosensor with electrochemically reduced graphene oxide, J. Electrochem. Soc. **165**(8), B3201 (2018), https://doi.org/10.1149/2.0261808jes

[9] A.A. Generalov, M.A. Andersson, X. Yang, A. Vorobiev, and J. Stake, A 400-GHz graphene FET detector, IEEE Trans. Terahertz Sci. Technol. **7**(5), 614–616 (2017), https://doi.org/10.1109/TTHZ.2017.2722360

[10] E. Javadi, D.B. But, K. Ikamas, J. Zdanevičius, W. Knap, and A. Lisauskas, Sensitivity of field-effect transistor-based terahertz detectors, Sensors **21**(9), 2909 (2021), https://doi.org/10.3390/s21092909

[11] S.M. Song and B.-J. Cho, Contact resistance in graphene channel transistors, Carbon Lett. **14**(3), 162–170 (2013), https://doi.org/10.5714/CL.2013.14.3.162

[12] F. Xia, V. Perebeinos, Y.-M. Lin, Y. Wu, and P. Avouris, The origins and limits of metal–graphene junction resistance, Nature Nanotechnol. **6**(3), 179–184 (2011), https://doi.org/10.1038/nnano.2011.6

[13] H. Zhong, Z. Zhang, B. Chen, H. Xu, D. Yu, L. Huang, and L. Peng, Realization of low contact resistance close to theoretical limit in graphene transistors, Nano Res. **8**(5), 1669–1679 (2015), https://doi.org/10.1007/s12274-014-0656-z

[14] K. Jia, J. Yang, Y. Su, P. Nie, J. Zhong, Q. Liang, and H. Zhu, Stability analysis of a back-gate graphene transistor in air environment, J. Semicond. **34**(8), 084004 (2013), https://doi.org/10.1088/1674-4926/34/8/084004

[15] D. Čibiraitė, M. Bauer, A. Lisauskas, V. Krozer, H.G. Roskos, A. Ramer, V. Krozer, W. Heinrich, S. Pralgauskaitė, J. Zdanevičius, J. Matukas, M. Andersson, and J. Stake, in: *Proceedings of the 2017 International Conference on Noise and Fluctuations (ICNF)* (IEEE, 2017) pp. 1–4, https://doi.org/10.1109/ICNF.2017.7986008

[16] J. Zdanevičius, D. Čibiraitė, K. Ikamas, M. Bauer, J. Matukas, A. Lisauskas, H. Richter, T. Hagelschuer, V. Krozer, H.-W. Hubers, and H.G. Roskos, Field-effect transistor based detectors for power monitoring of THz quantum cascade lasers, IEEE Trans. Terahertz Sci. Technol. **8**(6), 613–621 (2018), https://doi.org/10.1109/TTHZ.2018.2871360

[17] K. Ikamas, D. Cibiraite, A. Lisauskas, M. Bauer, V. Krozer, and H.G. Roskos, Broadband terahertz power detectors based on 90-nm silicon CMOS transistors with flat responsivity up to 2.2 THz, IEEE Electron Device Lett. **39**(9), 1413–1416 (2018), https://doi.org/10.1109/LED.2018.2859300

[18] M. Dyakonov and M. Shur, Detection, mixing, and frequency multiplication of terahertz radiation by two-dimensional electronic fluid, IEEE Trans. Electron. Dev. **43**(3), 380–387 (1996), https://doi.org/10.1109/16.485650

[19] A. Lisauskas, U. Pfeiffer, E. Öjefors, P. Haring Bolìvar, D. Glaab, and H.G. Roskos, Rational design of high-responsivity detectors of terahertz radiation based on distributed self-mixing in silicon field-effect transistors, J. Appl. Phys. **105**(11), 114511 (2009), https://doi.org/10.1063/1.3140611

[20] S. Boppel, A. Lisauskas, M. Mundt, D. Seliuta, L. Minkevičius, I. Kašalynas, G. Valušis, M. Mittendorff, S. Winnerl, V. Krozer, and H.G. Roskos, CMOS integrated antenna-coupled field-effect transistors for the detection of radiation from 0.2 to 4.3 THz, IEEE Trans. Microwave Theory Tech. **60**(12), 3834–3843 (2012), https://doi.org/10.1109/TMTT.2012.2221732

[21] M. Bauer, A. Rämer, S.A. Chevtchenko, K.Y. Osipov, D. Čibiraitė, S. Pralgauskaitė, K. Ikamas, A. Lisauskas, W. Heinrich, V. Krozer, and H.G. Roskos, A high-sensitivity AlGaN/GaN HEMT terahertz detector with integrated broadband bow-tie antenna, IEEE Trans. Terahertz Sci. Technol. **9**(4), 430–444 (2019), https://doi.org/10.1109/TTHZ.2019.2917782

[22] M. Shur, T.A. Fjeldly, T. Ytterdal, and K. Lee, Unified MOSFET model, Solid State Electron. **35**(12), 1795–1802 (1992), https://doi.org/10.1016/0038-1101(92)90263-C

[23] S. Das Sarma, S. Adam, E.H. Hwang, and E. Rossi, Electronic transport in two-dimensional graphene, Rev. Mod. Phys. **83**(2), 407–470 (2011), https://doi.org/10.1103/RevModPhys.83.407

[24] V. Ariel and A. Natan, *Electron Effective Mass in Graphene* (2012), https://arxiv.org/abs/1206.6100, https://doi.org/10.48550/ARXIV.1206.6100

[25] E. Tiras, S. Ardali, T. Tiras, E. Arslan, S. Cakmakyapan, O. Kazar, J. Hassan, E. Janzén, and E. Ozbay, Effective mass of electron in monolayer graphene: Electron-phonon interaction, J. Appl. Phys. **113**(4), 043708 (2013), https://doi.org/10.1063/1.4789385

[26] D.B. Davidson, *Computational Electromagnetics for RF and Microwave Engineering* (Cambridge University Press, Cambridge, New York, 2005).

[27] A. Zak, M.A. Andersson, M. Bauer, J. Matukas, A. Lisauskas, H.G. Roskos, and J. Stake, Antenna-integrated 0.6 THz FET direct detectors based on CVD graphene, Nano Lett. **14**(10), 5834–5838 (2014), https://doi.org/10.1021/nl5027309

[28] H. Wang, Y. Wu, C. Cong, J. Shang, and T. Yu, Hysteresis of electronic transport in graphene transistors, ACS Nano **4**(12), 7221–7228 (2010), https://doi.org/10.1021/nn101950n

[29] S. Rumyantsev, G. Liu, W. Stillman, M. Shur, and A.A. Balandin, Electrical and noise characteristics of graphene field-effect transistors: ambient effects, noise sources and physical mechanisms, J. Phys. Condens. Matter **22**(39), 395302 (2010), https://doi.org/10.1088/0953-8984/22/39/395302

[30] A.A. Balandin, Low-frequency $1/f$ noise in graphene devices, Nat. Nanotechnol. **8**(8), 549–555 (2013), https://doi.org/10.1038/nnano.2013.144

[31] T. Wu, A. Alharbi, T. Taniguchi, K. Watanabe, and D. Shahrjerdi, Low-frequency noise in irradiated graphene FETs, Appl. Phys. Lett. **113**(19), 193502 (2018), https://doi.org/10.1063/1.5051658

[32] X. Yang, A. Vorobiev, K. Jeppson, J. Stake, L. Banszerus, C. Stampfer, M. Otto, and D. Neumaier, in: *Proceedings of the 2018 43rd International Conference on Infrared, Millimeter, and Terahertz Waves (IRMMW-THz)* (2018) pp. 1–2, https://doi.org/10.1109/IRMMW-THz.2018.8510404

[33] M. Tian, Q. Hu, C. Gu, X. Xiong, Z. Zhang, X. Li, and Y. Wu, Tunable $1/f$ noise in CVD Bernal-stacked bilayer graphene transistors, ACS Appl. Mater. Interfaces **12**(15), 17686–17690 (2020), https://doi.org/10.1021/acsami.9b21070

[34] J.S. Moon, H.-C. Seo, M. Antcliffe, S. Lin, C. McGuire, D. Le, L.O. Nyakiti, D.K. Gaskill, P.M. Campbell, K.-M. Lee, and P. Asbeck,

Graphene FET-based zero-bias RF to millimeter-wave detection, IEEE Electron Device Lett. **33**(10), 1357–1359 (2012), https://doi.org/10.1109/LED.2012.2210184

[35] A. Rehman, J.A. Delgado Notario, J. Salvador Sanchez, Y.M. Meziani, G. Cywiński, W. Knap, A.A. Balandin, M. Levinshtein, and S. Rumyantsev, Nature of the 1/*f* noise in graphene–direct evidence for the mobility fluctuation mechanism, Nanoscale **14**, 7242–7249 (2022), https://doi.org/10.1039/D2NR00207H

[36] S. Pralgauskaitė, K. Ikamas, J. Matukas, A. Lisauskas, V. Jakštas, V. Janonis, I. Kašalynas, P. Prystawko, and M. Leszczynski, in: *Proceedings of the 2018 22nd International Microwave and Radar Conference (MIKON)* (IEEE, 2018) pp. 186–189, https://doi.org/10.23919/MIKON.2018.8405173

[37] A. Lisauskas, A. Rämer, M. Burakevič, S. Chevtchenko, V. Krozer, W. Heinrich, and H.G. Roskos, Terahertz emission from biased AlGaN/GaN high-electron-mobility transistors, J. Appl. Phys. **125**(15), 151614 (2019), https://doi.org/10.1063/1.5083838

[38] M. Bauer, M. Andersson, A. Zak, P. Sakalas, D. Čibiraitė, A. Lisauskas, M. Schröter, J. Stake, and H.G. Roskos, The potential for sensitivity enhancement by the thermoelectric effect in carbon-nanotube and graphene Tera-FETs, J. Phys. Conf. Ser. **647**(1), 012004 (2015), https://doi.org/10.1088/1742-6596/647/1/012004

[39] D.A. Bandurin, I. Gayduchenko, Y. Cao, M. Moskotin, A. Principi, I.V. Grigorieva, G. Goltsman, G. Fedorov, and D. Svintsov, Dual origin of room temperature sub-terahertz photoresponse in graphene field effect transistors, Appl. Phys. Lett. **112**(14), 141101 (2018), https://doi.org/10.1063/1.5018151

TERAHERCŲ DETEKTORIŲ SU GRAFENO LAUKO TRANZISTORIAIS OPTIMIZACIJA AUKŠTADAŽNĖS PILNUTINĖS VARŽOS ANTENOMIS

D. Vizbaras [a], K. Ikamas [a, c], S. Pralgauskaitė [a], J. Matukas [a], A.A. Generalov [d], A. Lisauskas [a, b]

[a] *Vilniaus universiteto Taikomosios elektrodinamikos ir telekomunikacijų institutas, Vilnius, Lietuva*
[b] *Aukšto slėgio fizikos instituto CENTERA laboratorijos, Varšuva, Lenkija*
[c] *Generolo Jono Žemaičio Lietuvos karo akademijos Logistikos ir gynybos technologijų vadybos mokslo grupė, Vilnius, Lietuva*
[d] *Suomijos techninių tyrimų centras VTT, Espas, Suomija*

Santrauka

Šiame darbe pateikiami terahercų detektorių su vieno sluoksnio grafeno lauko tranzistoriumi (GLT) tyrimų rezultatai. Ištirti detektoriai su trimis skirtingomis paviršinio tipo antenomis: peteliške, peteliške su perdavimo linijomis ir disku su plyšiu. Pasiūlytas sprendimas leido sukurti skirtingas aukštadažnės pilnutinės varžos suderinimo sąlygas. Skaičiuojant įtaisų jautrį buvo pritaikytas pusiau empirinis modelis, kuriame panaudoti fizikiniai parametrai, gauti išmatavus įtaisų elektrines charakteristikas, ir sumodeliuoti antenų elektrodinaminiai parametrai. Modeliavimo rezultatai palyginti su kambario temperatūroje 50–1250 GHz dažnių ruože išmatuotomis jautrio vertėmis. Geras eksperimentinių ir teorinių rezultatų sutapimas rodo, kad paskirstyto varžinio maišymo artinį sėkmingai galima taikyti ir vieno sluoksnio grafeno lauko tranzistoriams. Taip pat ištirtas detektorių stabilumas, parametrų priklausomybė nuo temperatūros bei įvertinta tranzistoriaus kanalo triukšmų kilmė. Darbe pateiktas rekordinis GLT terahercų detektorių optinis jautris ir efektinė triukšmų galia: atitinkamai, 80 V/W ir 111 pW/$\sqrt{\text{Hz}}$ ties 336 GHz dažniu kambario temperatūroje.